Ilter, Mehmet C.; Dowhuszko, Alexis A.; Vangapattu, Kiran K.; Hamalainen, Jyri; Wichman, Risto

Visible light communication-based positioning for indoor environments using supervised learning

Published in:
2020 IEEE Global Communications Conference, GLOBECOM 2020 - Proceedings

DOI:
10.1109/GLOBECOM42002.2020.9322577

Published: 01/01/2020

Document Version
Peer-reviewed accepted author manuscript, also known as Final accepted manuscript or Post-print

Visible light communication-based positioning for indoor environments using supervised learning

Mehmet C. Ilter[1], Alexis A. Dowhuszko[2], Kiran K. Vangapattu[3], Jyri Hämäläinen[3] and Risto Wichman[1]
[1]Department of Signal Processing and Acoustics, Aalto University, Espoo, Finland
[2]Centre Tecnològic de Telecomunicacions de Catalunya (CTTC/CERCA), Castelldefels (Barcelona), Spain
[3]Department of Communications and Networking, Aalto University, Espoo, Finland
Email: {mehmet.ilter, kiran.vangapattu, jyri.hamalainen, risto.wichman}@aalto.fi; alexis.dowhuszko@cttc.es

***Abstract*—This paper studies a novel way to estimate the position of an object in an indoor environment, using the Channel State Information (CSI) that a Visible Light Communication (VLC) system collects to maintain the link-level connectivity. First, supervised learning is applied to characterize, the effect that an object in variable but *known* positions has on the received optical wireless signal. Second, the trained classifier is used to estimate the new *unknown* positions that the object may take, making use of the instantaneous CSI that is used to equalize the data-carrying signal samples in reception. The practical validation of the proposed positioning approach was done with the aid of a software-defined VLC link based on OFDM, in which a copy of the intensity modulated signal coming from a Phosphor-converted LED is captured by Photodetectors (PDs) in different room locations. Then, the CSI of the VLC receiver is used to train a Random Forest classifier, which will predict the position of the object during the assessment phase. The performance evaluation of our experimental setting shows that the proposed VLC-based positioning approach can reach a *few centimeter accuracy*, provided that a proper training is executed, without the necessity of deploying a large number of PDs in the room, or adding a VLC receiver on the object to be tracked.**

***Index Terms*—Software-defined VLC, Indoor positioning, Optical OFDM, Supervised Learning, Random Forest.**

I. Introduction

Different technologies have been studied in the literature to support the implementation of positioning systems, and most of them are based on ultrasonic acoustic waves, as well as electromagnetic waves on infrared and Radio Frequency (RF) bands. From all these options, Global Navigation Satellite Systems (GNSS) such as GPS and Galileo have been mostly used for outdoor applications, whereas positioning systems that sense the RF signal coming from existing Wi-Fi, Bluetooth and Radio Frequency Identification (RFID) devices have been mainly proposed for indoors [1]. While the accuracy of the RF-based positioning is limited the density of wireless indoor nodes, the Visible Light Communication (VLC) infrastructure can be built as an integral part of the illumination system, enabling a higher density of available VLC nodes. Furthermore, VLC-based indoor positioning benefits from the rapid development of low-cost, high-sensitivity photodetector technology that can now detect very small signal variations [2].

VLC technology tackles most of the drawbacks that monitoring systems based on RF have, avoiding as well the privacy concerns that surveillance cameras with image-recognition processing create on citizens' privacy. For example, since visible light beams cannot propagate through opaque obstacles, they can be easily confined into the designated coverage area, enabling a more secure communication link while complicating the work of an hypothetical eavesdropper [3]. In addition, though VLC uses a portion of the electromagnetic spectrum that is licence-free by definition, it has also potential to establish *low-interference* optical wireless links when directive spot light fixtures are used [4]. Thanks to this, the stability of the communication link increases notably, and it is possible to detect minor changes of the received optical power, which implies much better positioning accuracy when compared to RF-based solutions [5]. Last but not least, the same infrastructure that is deployed for illumination and communication can be also used for Visible Light-based Positioning (VLP). We also note that this technology can be utilized in environments such as hospitals, where the use of RF is banned because it may create Electromagnetic Compatibility (EMC) problems [6].

Most of the VLP solutions reported so far in the literature consider that the object to-be-tracked is equipped with a sensor. Then, by measuring the optical power that reaches the Photodetector (PD), it is possible to extract relevant metrics that can be used to estimate the actual location of the object. Examples of these metrics are the Angle-of-Arrival (AoA), Received Signal Strength (RSS), Time-of-Arrival (ToA), and Time-Difference-of-Arrival (TDoA) [7]. For instance, a TDoA-based positioning solution was proposed in [8], where ceiling LED lamps were utilized as reference points. Similarly, the authors of [9] derived the Cramer-Ratio bound for a ToA-based VLP system. Color-based localization was developed in [10] by combining TDoA and RSS metrics, whereas a passive localization mechanism based on the channel impulse response from the PD to different LED light sources was presented in [11]. Lately, novel VLP solutions based on machine learning algorithms have been proposed to extract useful patterns from the complex optical wireless channel that is configured indoors. For example, the authors of [12] presented a localization mechanism using a Weighted K-nearest neighbor (WKNN) classifier, whereas the use of an Artificial Neural Network (ANN) was suggested in [13] to make reliable position estimations using the RSS as input features of the neural network. Finally, multiple classifier fusion localization mechanism were studied in detail in [14].

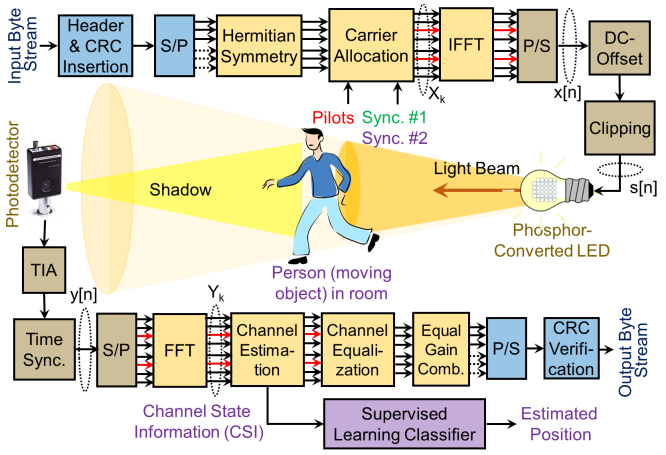

Fig. 1. Overview of VLC-based indoor positioning system. The Channel State Information that is collected at Channel Estimator output in reception is used for training the classifier. S/P: Serial-to-Parallel. P/S: Parallel-to-Serial. (I)FFT: (Inverse) Fast Fourier Transform. TIA: Transimpedance Amplifier.

Most of the VLP research reported so far in the literature uses the visible light signal only for positioning purposes, enabling to design an *ad hoc* waveform that is just suitable for this purpose. Yet, it would be more cost-effective to reuse the existing VLC infrastructure for positioning, rather than to build a separate VLP system in parallel. This is a key difference of the approach that is proposed in this paper, which falls under a sub-category that we named Visible Light Communication-based Positioning (VLCP). For the practical validation of our positioning approach, we implemented a software-defined VLC link based on OFDM, using Universal Software Radio Peripherals (USRPs), low-cost phosphor-converted LEDs [15], and commercial Photodetectors [16]. It is important to notice that the numerology of the Optical OFDM frame used in the experimental setting was designed to optimize the data rate of the VLCP system, rather than the positioning accuracy. Therefore, the Random Forest classifier was trained by employing Channel State Information (CSI) used to detect the transmitted data stream, and the performance of the VLC link is not impacted due the positioning feature that is added.

The rest of the paper is organized as follows: Section II describes the implemented software-defined VLC link, including the details of the signal processing that was utilized to obtain the CSI for indoor positioning. Section III addresses the key concepts behind the proposed Random Forest algorithm, and adapts it to the positioning task that is needed. Then, Section IV explains the experimental setting that was used to validate the VLCP concept, and carries out the performance evaluation when a sample object took different positions on a service area. Finally, conclusions are drawn in Section V.

II. Implementation Details of the VLC Link

The block diagram of the software-defined VLC link that used to collect the CSI to train the supervised learning classifier is shown in Fig. 1. The transmitter side of the VLC link consists of an Optical OFDM transmitter, which

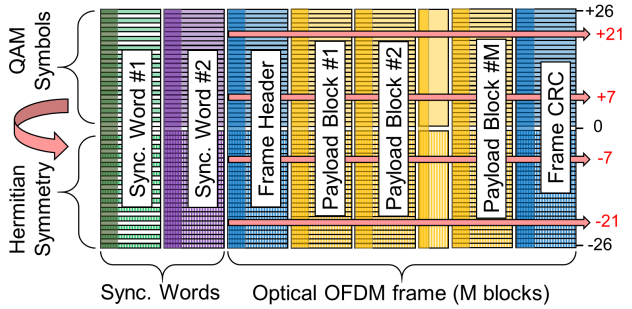

Fig. 2. Structure of the Optical OFDM frame used to acquire the CSI for indoor positioning, composed by two synchronization words, a frame header, M payload OFDM symbols, and a frame CRC. Note that CSI is estimated on a frame-by-frame basis, using the QAM training symbols on *Sync. Word #2*.

uses the input sequence of bytes to generate a unipolar real-valued signal that modulates the intensity of the LED light beam. At the receiver side, a PD is used to transform the time-varying optical signal into an electrical current, whose samples are then processed by the Optical OFDM receiver to estimate the original sequence of bytes that was transmitted. In the following subsections, further details are provided on the signal processing that is performed in transmission and reception.

A. Signal processing in the VLC transmitter

The input stream of bytes is divided into packets and, after that, a packet header is inserted and a Cyclic Redundancy Check (CRC) is appended. Then, bytes are divided into bits, and groups of bits are mapped onto $N/2-1$ constellation points. (*i.e.*, BPSK for the header and QPSK for the payload). After Serial-to-Parallel (S/P) conversion, the Hermitian Symmetric feature is introduced on the vector of size N that feeds the Inverse Fast Fourier Transform (IFFT), *i.e.*,

$$\mathbf{X} = [X_{N/2-1} \cdots X_1 \; X_0 \; X_{-1} \cdots X_{-N/2}]^{\mathrm{T}}, \qquad (1)$$

verifying

$$X_k = \begin{cases} X^*_{-k} & k = 1, \ldots, N/2-1, \\ 0 & k = 0, -N/2. \end{cases} \qquad (2)$$

This way, the time domain signal at the IFFT output, *i.e.*,

$$x[n] = \frac{1}{\sqrt{N}} \sum_{k=-N/2}^{N/2-1} X_k \exp\left(\mathrm{j}\frac{2\pi k n}{N}\right), \quad n = 0, \ldots, N-1, \qquad (3)$$

becomes real-valued (*i.e.*, imaginary part is always zero). Note that zero-padding can be used on the subcarriers with highest and lowest indexes, such that the bandwidth of the OFDM signal is adjusted to the one that the LED can support.

Pilot signals are also inserted, as well as two synchronization words that are utilized by the OFDM receiver for frame synchronization and channel estimation purposes. More precisely, *Sync. Word #1* is used to synchronize in time the received signal samples and to perform a coarse frequency correction that is common to all subcarriers. In time domain, this synchronization word consists of two repeated parts, and is obtained by allocating random BPSK training symbols on the subcarriers with *even* indexes in (2), while leaving unused

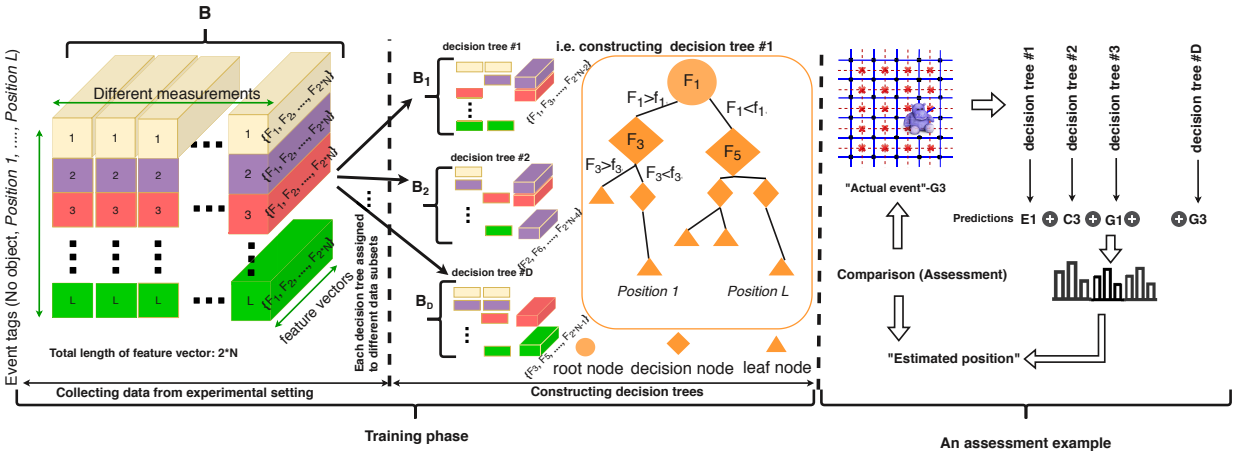

Fig. 3. The construction of the decision trees in the Random Forest algorithm takes advantage of the labeled data during the training phase (supervised learning), whereas the decision-making phase identifies the most likely location that collects most votes at the output of each decision tree.

the remaining subcarriers with *odd* indexes. On the other hand, *Sync. Word #2* contains random QPSK training symbols, which are known *a priori* in reception to estimate the channel gains per subcarrier on a frame-by-frame basis.

Finally, after Parallel-to-Serial (P/S) conversion, a Cyclic Prefix (CP) is added, and the resulting signal is DC-biased and Clipped to obtain

$$s[n] = \begin{cases} x[n] + x_{\mathrm{dc}} & \text{for } x[n] + x_{\mathrm{dc}} \geq 0 \\ 0 & \text{for } x[n] + x_{\mathrm{dc}} < 0 \end{cases}, \qquad (4)$$

which is used to modulate the Intensity of the LED light beam.

Without loss of generality, we assume that the IFFT size is $N = 64$, that pilot symbols are placed on subcarriers indexes ± 7 and ± 21, and that zero-padded is used on the five upper- and lower-most subcarriers (*i.e.*, with indexes $\pm 27, \ldots, \pm 31$). This enables us to accommodate up to 24 QAM symbols per payload OFDM symbol, as it can be appreciated in the Optical OFDM frame structure that is illustrated in Fig. 2.

B. Signal processing in the VLC receiver

The optical signal that reaches the VLC receiver is transformed into an electrical current by the Photodetector (PD) and then, it is converted into an analogous voltage by the Transimpedance Amplifier (TIA). The digitalized samples of this signal are fed into the time synchronization block, which is responsible for identifying the location of *Sync.,Word,#1* that marks the beginning of the OFDM frame. Then, the CP from each OFDM symbol is removed, S/P conversion is performed, and an N-point FFT processing is applied, *i.e.*,

$$Y_k = \frac{1}{\sqrt{N}} \sum_{n=0}^{N-1} y[n] \exp\left(-\mathrm{j}\frac{2\pi k n}{N}\right), k = \pm 1, \ldots, \pm\frac{N}{2} - 1. \qquad (5)$$

Then, received samples associated to *Sync. Word #2* are fed into the Channel Estimation block to obtain the CSI associated to the different subcarrier indexes. This information, which is used to perform the equalization of the OFDM symbols for the Header, Payload and CRC parts of the frame, will be also used by the supervised learning classifier to estimate the position of the obstacle that lies between the LED and the PD. Finally, Equal Gain Combining is applied, *i.e.*,

$$\widetilde{Y}_k = \left(Y_k + Y_{-k}^*\right)/\sqrt{2}, \qquad k = 1, \ldots, N/2 - 1, \qquad (6)$$

to exploit the Hermitian Symmetric structure of the vector of transmitted QAM symbols, before P/S conversion, QAM demodulation, and CRC verification are performed.

III. Random Forest Algorithm

Random Forest [17] is a supervised learning algorithm in which a collective learning process is carried out in a group of decision trees. Each decision tree is trained by a different segment of complete labeled training data, which takes into account a random feature subset in a process that is known as *Random Feature Selection*. To do so, each decision tree uses a different feature subset during the training phase, aiming at reducing the correlation among individual decision trees during the assessment phase. During assessment, the final decision is determined by the plurality voting, and the alternative with highest number of votes becomes a final decision. An overview of this process is illustrated in Fig. 3.

During the training phase, each decision tree is constructed using the assigned labeled data and the corresponding random feature subset. Entries in this situation are the CSI amplitude and the tag that identifies its associated event. For each measurement with a given event tag, the feature set consists of a $2N$-length feature vector when two PDs are used for VLCP. A decision tree contains a root node, multiple decision nodes, and multiple leaf nodes. The categorization of these nodes is defined by the splitting rule, which stems from the Shannon entropy formula, *i.e.*,

$$H = -\sum_i p_i \log_2(p_i), \qquad (7)$$

where p_i is the probability of i-th discrete event that is being considered during the experiment. This entropy is calculated each time, before and after tree splitting, and the difference between the two entropies yield to the expected Information Gain (IG) from that split.

The feature that brings the largest IG is chosen by the root node and, for the remaining features, a similar splitting is

Algorithm 1: Pseudo-code for constructing D different decision trees in the Random Forest classifier *training* phase.

Input: Number of decision trees: D
Total training data with labels:
$\mathbf{B} = [\mathbf{B}_1, \mathbf{B}_2, \ldots, \mathbf{B}_D]$
Feature set (with random subsets):
$\mathbf{F} = \{\mathbf{F}_1, \mathbf{F}_2, \ldots, \mathbf{F}_D\}$
Event tags:
$\Omega = \{\text{no object, position } 1, \ldots, \text{position } L\}$
The number of total event tags ($|\Omega|$): $L + 1$.

for $d = 1 : D$ **do**
- Select randomly a subset of labeled training data-$\mathbf{B}_d$
- **(a)** Use a subset of the feature subset-$\mathbf{F}_d$
- **(b)** Find the best splitting rule and root node based on $\mathbf{B}_d$, by using $\mathbf{F}_d$ and (7)
- **(c)** Split a node using the best split features and values
- **(d)** Repeat (b) and (c) until all leaf nodes are reached

return D individual decision trees, trained for $L + 1$ event tags, and ready for the assessment phase;

done until the correct decision is reached, which takes place when the correct event labelling of the leaf node is found. This processes is summarized in Algorithm 1.

IV. VLCP SYSTEM

The *signature* that the object that is placed between the LED and PD creates on the CSI amplitudes is used to train the decision trees of the Random Forest algorithm. To illustrate this concept, Fig. 4 shows the CSI amplitudes that were collected during a given 10-sec measurement, assuming that the object is placed on two different locations: a) Position *A1*, which is far away from the Line-of-Sight (LoS) link between LED and PD 1 and PD 2, respectively. b) Position *I4*, which is far away from the LoS link between LED and PD 1, but close enough to the LoS link between LED and PD 2.

Each of these CSI plots can be sub-divided into two 5-sec. parts described as follows: In the first part, there is no object and the CSI accounts the combined effect that the LoS link and the flat surface of the table have on the

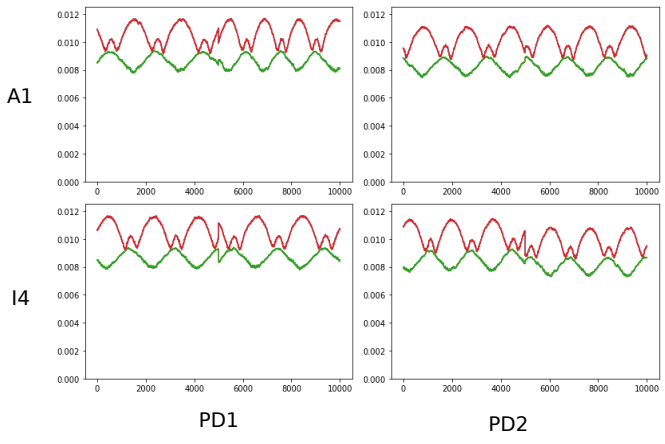

Fig. 4. Signatures that the object introduces on the CSI amplitudes acquired from pilot symbols placed on subcarriers $k = \pm 21$ (green lines) and $k = \pm 7$ (red lines) at PD 1 (left panel) and PD 2 (right panel). Upper plots: Object is placed on position $A1$. Lower plots: Object is placed on position $I4$.

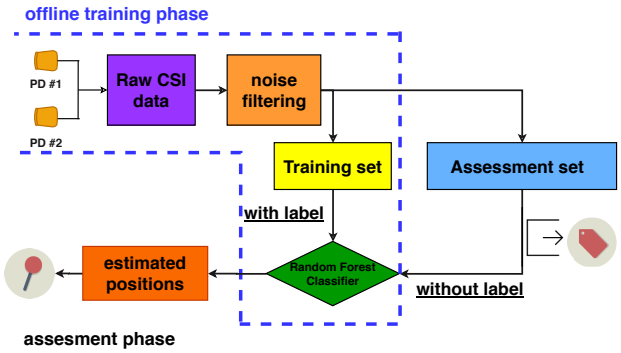

Fig. 5. Block diagram of the process used to evaluate the accuracy of proposed VLCP solution. The input CSI samples with labels (known positions) are used to train *offline* the Random Forest classifier, whereas the unlabeled CSI inputs are used in the *online* assessment phase to estimate the position of the object.

received VLC signal. On the other hand, in the second part, the object is placed at the labeled position on the table, and the CSI also accounts the impact of the object on the VLC channel. As it can be also appreciated in Fig. 4, different subcarriers experience different CSI amplitudes for the same object, and CSI amplitudes vary from object to object in the same subcarrier, creating a *hidden* signature that the Random Forest algorithm aim at modeling. The overall process of the VLCP proposal is shown in Fig. 5, where the *offline* training phase and the *online* assessment phase of the Random Forest classifier are identified.

The practical validation of the VLCP proposal was done on a controlled experimental setting, which resembles the one found in realistic indoor environments when doing a proper dimension-scaling. In this experimental setup, one Phosphor-Converted (PC)-LED and two PDs are placed on the opposite sides of a meeting-room table of size 240 cm $\times$ 120 cm, as illustrated in Fig. 6 and Fig. 7. In the central part of the table, a grid with 5×4 square elements of size 30 cm $\times$ 30 cm is marked (solid blue lines in the figure), creating 30 equal-separated positions that are used to train the Random Forest classifiers (solid black points in the figure). Finally, the center of each of these square elements are used to assess the performance of the classifier after the training phase is over (red crosses in the figure). It is important to highlight the boresight direction of the PC-LED points to position *K3*, whereas the boresight directions of the PDs are pointing directly towards the PC-LED. Finally, it is important to highlight that the sampling rate and size of the payload (M) of the software-defined VLC link was selected such that the electrical bandwidth of the OFDM signal becomes 1 MHz, and 1000 CSI samples are collected per sec.

A. Offline training phase

In the process of creating the dataset to train the Random Forest classifier, 30000 CSI samples are collected when the object is placed on the positions of Fig. 6 marked with a solid black point. Each of these samples consists of 128 different CSI amplitudes (64 CSI values per PD), which are obtained from the N subcarriers of the Optical OFDM signal.

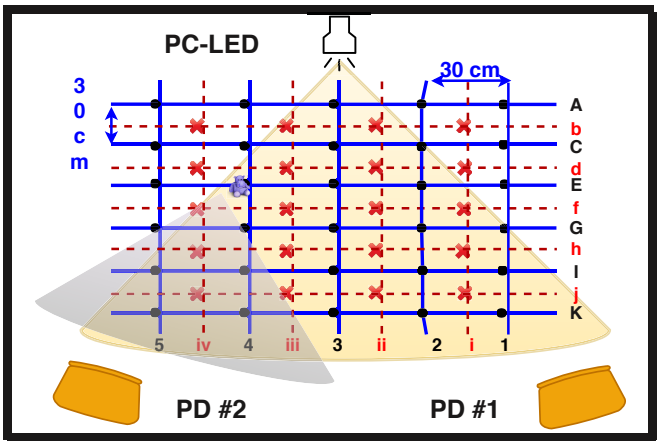

Fig. 6. Experimental setting used in the evaluation of the VLCP performance. PC-LED and the two PDs are placed on the opposite sides of a meeting-room table of size 240 cm × 120 cm. A square grid with 30 cm × 30 cm elements is marked in the center of the table to collect the CSI data with labels for training (solid black points), whereas the unlabeled CSI for assessment is collected on the center of each of these blue squares elements (red crosses).

To mitigate the impact of measurement noise in the training data, a Moving Average (MA) time-filtering was applied to the CSI amplitudes per subcarrier using a window length of 100. In the *labeled* input for training phase, each time instant/snapshot was associated with an event tag taken from set $\Omega = \{\text{no object, position } A1, \text{ position } A2, \ldots, \text{position } K5\}$. Moreover, part of the collected CSI was also reserved to be used as *unlabeled* data for the performance assessment of the classifier during the decision-making phase. The *training ratio* is the fraction of the whole available data that is used exclusively for training; the remaining data is used for assessment. During the training phase, the Random Forest classifier identifies hidden patterns on the collected CSI sequences for the different objects, taking advantage of the labels that were included while doing the measurements. To do so, 64 different amplitude values are introduced as total feature set of the Random Forest Classifier, along with corresponding position labels. In order to utilize the statistical ability of the Random Forest classifier, which can assign optimal weights for the 64 features, all features are initialized with equal weights. During the training phase, 200 decision trees are constructed in total.

Each measurement took 10 sec. and consisted of two parts: No object (5 sec.) and object at given position (5 sec.). During the first part., the CSI in absence of object was collected by the VLC receiver. Then, the selected object was located at a training position marked with a capital-letter-plus-number in Fig. 6, and the CSI in presence of object was obtained. In order to assess the performance of the Random Forest classifier, each measurement was repeated three times for each training location. Note that during the whole 10-sec. measurement window, the data transmission over the VLC link is maintained without interruption, as the object does not block completely the reception of the VLC signal.

B. Performance assessment

The performance assessment of our proposed VLCP solution considers two situations: On one hand *Case-1*, where the CSI collected from the 30 training positions - marked with solid black points in Fig. 6 - are used in the construction (training) and evaluation (assessment) of the Random Forest classifier. On the other hand *Case-2*, where the trained Random Forest classifier is evaluated when feeding its input with the CSI that is collected when the object takes any of the 20 new positions for assessment - marked with red crosses in Fig. 6.

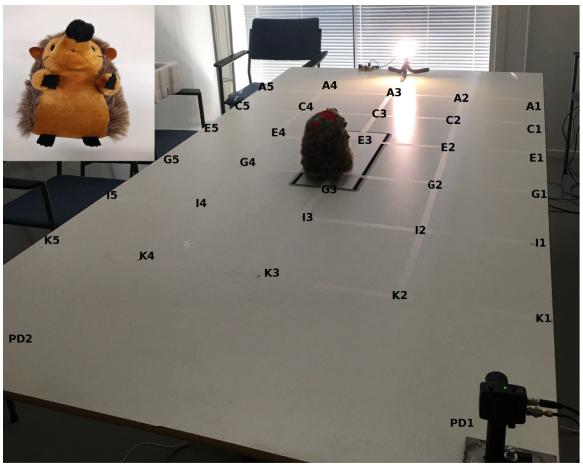

Fig. 7. Picture of the actual setting used in the experimental evaluation. The object that was used to identify its position on the table was a stuffed toy (brown hedgehog), whose shape can be approximated as a cylinder of diameter 8 cm and height of 22 cm. The points labeled with letters and numbers are the positions used in the training phase (here, hedgehog is on position $G3$).

In order to assess the performance of the Random Forest classifier, confusion matrices and Root Mean Square (RMS) positioning errors are considered. Confusion matrices are widely used to indicate the accuracy of a given classifier. In a confusion matrix, the values stored in the main diagonal corresponds to probability of making good predictions (hitting probability), whereas the off-diagonal values identify the probability of making wrong predictions (confusion probability). Since it is not practical to visualize the 30×30 confusion matrix that corresponds to all possible values in *Case-1*, a subset of them has been selected for visualization in Fig 8. Based on the confusion values when assessing the trained classifier with the CSI collected when object was placed on points in column *3* (upper table) and row *E* (lower table), it is possible to see that the Random Forest classifier can identify the presence of the object and estimate its position correctly in more than 98% of the cases. Similar hitting probabilities were observed in the remaining rows and columns of Fig. 6.

Finally, the RMS positioning error when the object is placed on the new assessment points - marked with red crosses in Fig. 6 - is calculated from the Euclidean distances that exists between the actual coordinates $(x_{l,0}; y_{l,0})$ for the object when placed in *assessment locations* l, and the estimated coordinates $(\widehat{x}_{l,i}; \widehat{y}_{l,i})$ that the trained classifier provides for the object in position l during measurement snapshot $i = 1, \ldots, I$, *i.e.*,

$$\text{RMSE}\,(x_{l,0}; y_{0,l}) = \sqrt{\frac{\sum_i \left(x_{l,0} - \widehat{x}_{l,i}\right)^2 + \left(y_{l,0} - \widehat{y}_{l,i}\right)^2}{I}}. \quad (8)$$

"Actual Positions"	"Estimated Positions"						
	No Object	A3	C3	E3	G3	I3	K3
No Object	0,999	0.00	0.00	0,0002	0,0007	0.00	0.00
A3	0.0004	0,999	0.00	0.00	0.00	0.00	0.00
C3	0,0005	0.00	0,995	0.00	0.00	0.00	0.00
E3	0,0001	0.00	0.00	0,992	0.00	0.00	0.00
G3	0.00	0.00	0.00	0.00	0,995	0.00	0.00
I3	0,0001	0.00	0.00	0.00	0.00	0,992	0.00
K3	0,0001	0.00	0.00	0.00	0.00	0.00	0,997

(a)

"Actual Positions"	"Estimated Positions"					
	No Object	E1	E2	E3	E4	E5
No Object	0,999	0.00	0,0003	0.00	0.00	0.00
E1	0,00088	0,9991	0.00	0.00	0.00	0.00
E2	0,0002	0.00	0,9993	0.00	0.00	0.00
E3	0,0004	0.00	0.00	0,9995	0.00	0.00
E4	0,0006	0.00	0.00	0.00	0,9993	0.00
E5	0,001	0.00	0.00	0.00	0.00	0,9986

(b)

Fig. 8. Confusion matrices obtained by the Random Forest classifier of the proposed VLCP solution when using a 70% training ratio. Upper table: Object takes positions on column *3*. Lower table: Object takes position on row *E*.

In total, $I = 5000$ CSI measurements were used to compute the RMS positioning error that corresponds for each of these assessment positions, which were not used in the training phase. According to the RMS errors reported in Fig. 9 for assessment positions, we conclude that the Random Forest classifier can estimate the position of the object with an accuracy that is similar to the separation between points used in the training phase (*i.e.*, less than 30 cm on average). If better positioning accuracy is desired, the Random Forest classifier should be trained with more densely packed training points.

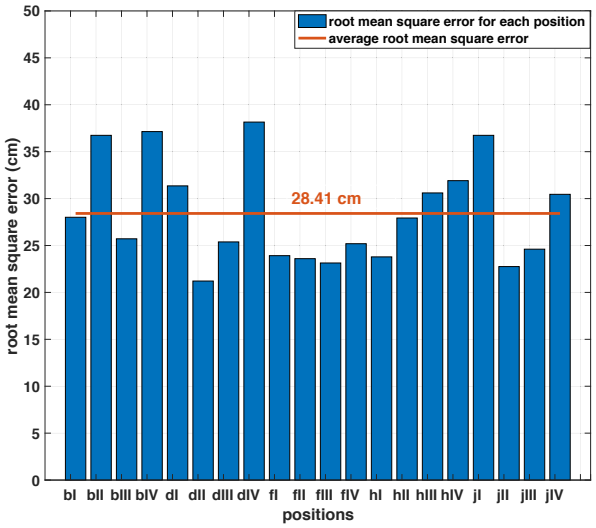

Fig. 9. RMS error of proposed VLCP solution when the object (brown hedgehog) takes different positions between the training points. As expected, the accuracy varies slightly with the position that the object takes, and is in most cases lower than the separation between training points (30 cm).

V. Conclusion

This paper validated the VLCP concept, in which the presence of an object was identified with the aid of a Random Forest classifier trained with the CSI that was collected from an ongoing VLC data transmission. More precisely, a software-defined Optical OFDM link was implemented, using commercial phosphor-converted LED and Photodetectors, and defining an OFDM frame structure that focused solely on the data rate requirements of the VLC system. The Random Forest classifier was trained using the CSI that was collected when a sample object was placed in 30 different positions between the LED and PD. VLCP system was able to identify the location of the object correctly in more than 98% of the cases. Moreover, when placing the object in new positions that were not used during the training phase, the RMS positioning error did not increase notably. The good accuracy that VLCP showed paves the way for its implementation in cases where RF-based positioning systems cannot be used.

Acknowledgment

This work has received funding from the Ministry of Science, Innovation, and Universities of Spain under Project TERESA-TEC2017-90093-C3-1-R (AEI/FEDER, UE), from the Catalan government under grant 2017-SGR-1479, and from the ATTRACT project funded by the EC under Grant Agreement 777222.

References

[1] F. Zafari, A. Gkelias, and K. Leung, "A survey of indoor localization systems and technologies," *IEEE Commun. Surv. Tutorial*, vol. 21, no. 3, pp. 2568–2599, Apr. 2019.

[2] L. Matheus, A. Vieira, L. Vieira, M. Vieira, and O. Gnawali, "Visible light communication: Concepts, applications and challenges," *IEEE Commun. Surveys Tuts.*, vol. 21, no. 4, pp. 3204–3237, Apr. 2019.

[3] A. Mostafa and L. Lampe, "Enhancing the security of VLC links: Physical-layer approaches," in *Proc. IEEE Summer Topicals Meeting Series*, July 2015, pp. 39–40.

[4] A. Dowhuszko and A. Pérez-Neira, "Achievable data rate of coordinated multi-point transmission for visible light communications," in *Proc. IEEE Int. Symp. on Personal Indoor and Mobile Radio Commun.*, Oct. 2017, pp. 1–7.

[5] J. Armstrong, Y. Sekercioglu, and A. Neild, "Visible light positioning: A roadmap for international standardization," *IEEE Commun. Mag.*, vol. 51, no. 12, pp. 68–73, Dec. 2013.

[6] K. Ishida, T. Fujioka, T. Tomomi, T. Endo, R. Hosokawa, T. Fujisaki, R. Yoshino, and M. Hirose, "Evaluation of electromagnetic fields in a hospital for safe use of electronic medical equipment," *Journal of Medical Systems*, vol. 40, no. 3, p. 46, Mar. 2016.

[7] A. Rahman, T. Li, and Y. Wang, "Recent advances in indoor localization via visible lights: A survey," *Sensors*, vol. 20, no. 5, p. 1382, Mar. 2020.

[8] S. Jung, S. Hann, and C. Park, "TDoA-based optical wireless indoor localization using led ceiling lamps," *IEEE Trans. Consumer Electronics*, vol. 57, no. 4, pp. 1592–1597, Nov. 2011.

[9] T. Wang, Y. Sekercioglu, A. Neild, and J. Armstrong, "Position accuracy of time-of-arrival based ranging using visible light with application in indoor localization systems," *Journal of Lightwave Technology*, vol. 31, no. 20, pp. 3302–3308, Sept. 2013.

[10] S. Pergoloni, Z. Mohamadi, A. Vegni, Z. Ghassemlooy, and M. Biagi, "Visible light indoor positioning through colored LEDs," in *Proc. IEEE Int. Conf. Commun. Workshops*, May 2017, pp. 150–155.

[11] K. Majeed and S. Hranilovic, "Performance bounds on passive indoor positioning using visible light," *Journal of Lightwave Technology*, vol. 38, no. 8, pp. 2190–2200, Apr. 2020.

[12] N. Faulkner, F. Alam, M. Legg, and S. Demidenko, "Watchers on the wall: Passive visible light-based positioning and tracking with embedded light-sensors on the wall," *IEEE Trans. Instrumentation and Measurement*, vol. 69, no. 5, pp. 2522–2532, Nov. 2019.

[13] S. Ni, F. Wang, S. Han, J. Pang, and S. You, "Two methods of accurate indoor positioning based on visible light communication system and artificial neural network," in *Proc. Int. Conf. Optical Commun. and Networks*, Aug. 2019, pp. 1–3.

[14] X. Guo, S. Shao, N. Ansari, and A. Khreishah, "Indoor localization using visible light via fusion of multiple classifiers," *IEEE Photonics Journal*, vol. 9, no. 6, pp. 1–16, Dec. 2017.

[15] Lumileds, "LUXEON Rebel PLUS — The original high power LED," July 2017, dS107 LUXEON Rebel PLUS Product Datasheet, url: https://www.lumileds.com/uploads/380/DS107-pdf.

[16] Thorlabs, "PDA100A2 Si switchable gain detector – User guide," May 2019, url: https://www.thorlabs.com/.

[17] L. Breiman, "Random forests," *Machine learning*, vol. 45, no. 1, pp. 5–32, 2001.